

1                   **Unsupervised clustering of Southern Ocean Argo float**  
2                   **temperature profiles**

3                   **Daniel C. Jones<sup>1</sup>, Harry J. Holt<sup>1,2</sup>, Andrew J.S. Meijers<sup>1</sup>, Emily Shuckburgh<sup>1</sup>**

4                                           <sup>1</sup>British Antarctic Survey, Cambridge, UK

5                                           <sup>2</sup>Department of Physics, University of Cambridge, Cambridge, UK

6                   **Key Points:**

- 7                   • We apply Gaussian mixture modeling (GMM) to Southern Ocean temperature data
- 8                   • GMM identifies spatially coherent profile types without using latitude or longitude
- 9                   information
- 10                  • GMM offers a complementary approach for objectively classifying temperature pro-
- 11                  files

---

Corresponding author: D. C. Jones, [dannes@bas.ac.uk](mailto:dannes@bas.ac.uk)

**Abstract**

The Southern Ocean has complex spatial variability, characterized by sharp fronts, steeply tilted isopycnals, and deep seasonal mixed layers. Methods of defining Southern Ocean spatial structures traditionally rely on somewhat ad-hoc combinations of physical, chemical, and dynamic properties. As a step towards an alternative approach for describing spatial variability in temperature, here we apply an unsupervised classification technique (that is, Gaussian mixture modelling or GMM) to Southern Ocean Argo float temperature profiles. GMM, without using any latitude or longitude information, automatically identifies several spatially coherent circumpolar classes influenced by the Antarctic Circumpolar Current. In addition, GMM identifies classes that bear the imprint of mode/intermediate water formation and export, large-scale gyre circulation, and the Agulhas Current, among others. Because GMM is robust, standardized, and automated, it can potentially be used to identify structures (such as fronts) in both observational and model datasets, possibly making it a useful complement to existing classification techniques.

**Plain Language Summary**

The Southern Ocean is an important part of the climate system, in part because it absorbs a large fraction of the heat and carbon that is added to the atmosphere/ocean system by human-driven fossil fuel burning. In this work, we use a machine learning technique to automatically sort Southern Ocean temperature measurements into groups based on how those temperature measurements change with depth. Different groups have the fingerprints of different large-scale circulation patterns, such as the powerful Antarctic Circumpolar Current that flows around Antarctica. The groups that we identify are consistent with our understanding of the Southern Ocean, which gives us confidence that our machine learning technique may be useful for automatically grouping measurements and computer model data in the future. This matters because the climate science community needs a new set of tools, possibly including the machine learning technique that we use in this paper, to deal with a very large, ever-increasing volume of observational and computer model data.

## 1 Introduction

The Southern Ocean (SO) is a critical component of Earth's climate system, having thus far absorbed greater than 75% of the energy added via anthropogenic emissions and 50% of the excess carbon [Fletcher *et al.*; Frölicher *et al.*, 2015]. Its ability to absorb heat and carbon comes in part from its unique spatial structure and circulation, which features upwelling of cold, nutrient rich waters and regions of dense water formation [Lumpkin and Speer, 2007]. Characterizing and understanding the spatial variability of the SO remains an important and climatically-relevant goal of modern oceanography.

Through decades of effort, the oceanographic community has converged on a description of ocean spatial variability that uses temperature, salinity, dynamical, and biogeochemical patterns to define different spatial structures [Emery, 2003; Talley, 2013, and references therein]. For example, SO mode waters, located equatorward of the Antarctic Circumpolar Current (ACC), are commonly identified using potential vorticity minima and ranges of neutral density [Hanawa and Talley, 2001; Sallée *et al.*, 2008, 2010a; Herraiz-Borreguero and Rintoul, 2011]. Such systematic approaches employ the understanding that structural properties are "set" in their formation regions and modified by advection, mixing, and biogeochemical processes. In the SO, classification in latitude-longitude has traditionally been centered around several fronts of the ACC, defined by sharp transitions in sea surface height or neutral density [Kim and Orsi, 2014]. The classical southern boundary of the ACC (SBDY) marks the transition between subpolar, gyre-dominated circulations and lower-latitude, more circumpolar flow. The ACC itself features three circumpolar fronts, namely the southern ACC front (SACCF), the Polar Front (PF), and the Subantarctic Front (SAF) [Orsi *et al.*, 1995]. These three fronts separate the subpolar SO from the subtropical domain [Naveira-Garabato *et al.*, 2011].

The modern, property-driven classification scheme is extremely useful and will continue to be useful well into the future, but it is not necessarily ideal for every application. Many of the temperature, salinity, and density values used to delimit one structure from another are somewhat ad-hoc and very specific (e.g. boundaries between different types of mode water). These schemes are useful for observational data analysis but difficult to apply to numerical models of the ocean, which do not necessarily feature exactly the same structure as the observed ocean [Sallée *et al.*, 2013]. In addition, traditional classification approaches that define structures by specific property ranges are limited by the fact that these proper-

71 ties may change over time, either as long-term trends (for example, the warming of Antarctic  
72 Bottom Water observed by *Purkey and Johnson* [2010]) or in terms of interannual variability  
73 [*Naveira-Garabato et al.*, 2009]. We suggest that it is prudent to develop and test alternative  
74 methods for the classification of oceanic temperature, salinity, and density structures, as a  
75 complement to existing expertise-driven methods.

76 *Maze et al.* [2017] have shown that Argo temperature profile data from the North At-  
77 lantic Ocean can be usefully grouped into classes using Gaussian mixture modelling (GMM),  
78 an unsupervised classification technique. GMM describes the spatial structure of Argo pro-  
79 files as a collection of Gaussian modes whose means and standard deviations generally vary  
80 with pressure. In this work, we apply GMM to Southern Ocean Argo temperature profiles  
81 in the upper 1000 m of the water column. We find that GMM identifies several circumpolar  
82 classes, gyres, the Agulhas current, and pathways broadly associated with the formation and  
83 export of mode and intermediate waters. In section 2, we describe the Argo dataset and the  
84 basics of GMM. In section 3, we present the results of applying GMM to Southern Ocean  
85 Argo data, and in sections 4 and 5 we offer a brief discussion and summarize our conclu-  
86 sions.

## 87 **2 Methods**

88 We applied an unsupervised classification method (i.e. Gaussian mixture modelling,  
89 hereafter GMM) to Southern Ocean Argo float data. In this section, we briefly describe the  
90 Argo dataset and the basics of GMM. We use the *scikit-learn* machine learning library for  
91 Python (<http://scikit-learn.org/>), and the source code used for much of the analy-  
92 sis in this paper is available via Github [*Holt and Jones*, 2018]. We refer the reader to *Maze*  
93 *et al.* [2017] for further detail on applying GMM to Argo float data.

### 94 **2.1 Argo float dataset**

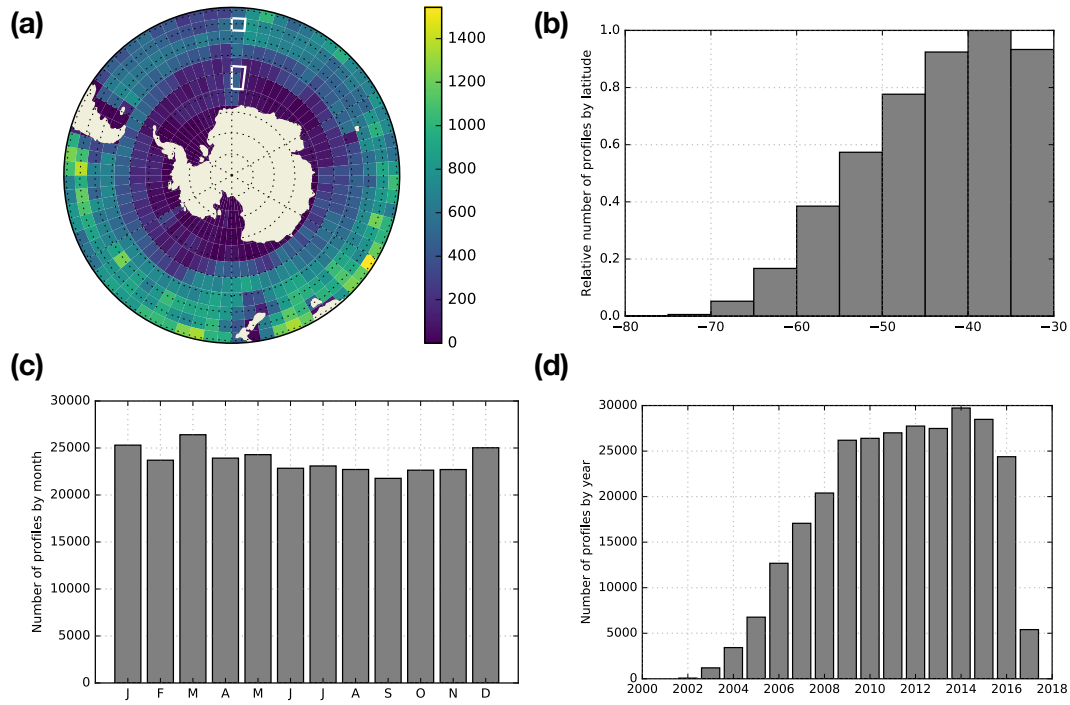
95 Argo floats are autonomous ocean instruments that measure, at minimum, the tempera-  
96 ture and salinity of the ocean by periodically taking vertical profiles. Every 10 days, starting  
97 at a “neutral” position of 1000 m, an Argo float dives down to 2000 m before rising to the  
98 surface, taking a vertical profile of the water column along the way. The measurements are  
99 transmitted via satellite and are ultimately made freely available via the Argo Global Data  
100 Assembly Centers (GDACs) after some quality control checks. At the time of this writing,

101 over 3800 Argo floats are active in the global ocean, producing over 100,000 temperature and  
102 salinity profiles per year with an average spacing of  $3^\circ$  (<http://www.argo.ucsd.edu/>).

103 For this study, we selected all available Argo profiles south of  $30^\circ\text{S}$  that have been  
104 flagged by the GDACs as “observation good” (i.e. quality control flag = 1) covering the time  
105 period from 2001 to early 2017. More specifically, we used a vertically interpolated product  
106 with 400 equally spaced pressure levels ranging from 5 to 2000 dbar in 5 dbar increments.  
107 After discarding profiles with greater than or equal to 6% NaN values (2% of the initial num-  
108 ber of profiles) and discarding pressure levels with greater than or equal to 3% NaN values,  
109 we were left with 284,427 profiles, each with 192 pressure levels between 15 dbar and 980  
110 dbar. Most of these initially removed NaN values came from interpolation below roughly  
111 1000 dbar, as opposed to gaps in the original dataset. We selected our NaN cut-off values  
112 based on the relatively large increase in the number of NaN values below 1000 dbar. We re-  
113 placed all remaining NaN values ( $\ll 1\%$  of the total temperature measurements) with lin-  
114 earlyly interpolated estimates using nearest neighbor values with respect to pressure. We refer  
115 to the resulting dataset as the cleaned dataset.

116 Because of the autonomous and free-drifting nature of the floats, the profiles are not  
117 distributed evenly in latitude/longitude (Figure 1). The profiles are more heavily concen-  
118 trated in the Pacific sector (roughly 890 profiles per degree longitude, totalling 47% of pro-  
119 files) and Indian sector (800 profiles per degree longitude, totalling 34% of profiles), with  
120 relatively fewer profiles in the Atlantic sector (610 profiles per degree longitude, 19% of  
121 total). When counted in equal-area bins and plotted by latitude, we see that the number of  
122 profiles decreases towards Antarctica (Figure 1(b)), which is partly due to challenging oper-  
123 ational conditions associated with seasonal sea ice, which can extend to just north of  $60^\circ\text{S}$   
124 at maximum areal extent. The profiles are slightly over-represented in the Austral summer  
125 and autumn (DJF-MAM, 52% of profiles) and under-represented in the Austral winter and  
126 spring (JJA-SON, 48% of profiles), and the number of profiles increases until 2013 (Figure  
127 1(c,d)). Since we selected an Argo dataset that was created in early 2017, there are relatively  
128 few profiles from that year.

133 The profiles selected for this study display a large variety of vertical temperature struc-  
134 tures (Figure 2). The range of temperatures is wider in the surface and considerably narrower  
135 with increasing pressure, in part reflecting the seasonal cycle in upper ocean temperatures. A  
136 large number of profiles feature colder temperatures near the surface and warmer tempera-

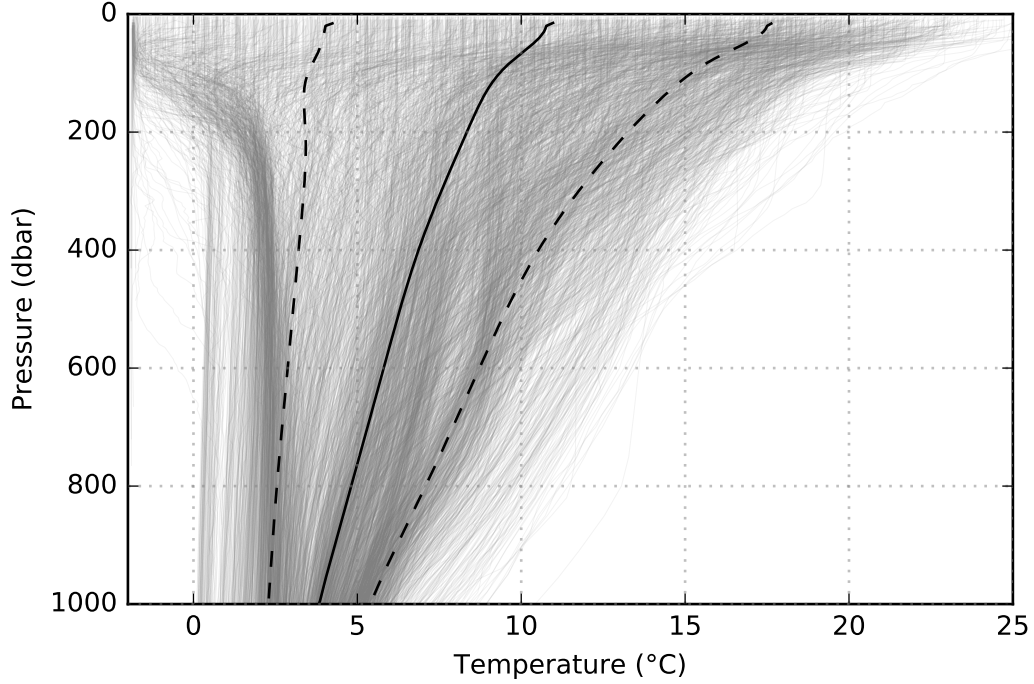


129 **Figure 1.** Distribution of Argo temperature profiles from the cleaned dataset. (a) Number of profiles in  
 130  $5^\circ \times 5^\circ$  bins. Two equal-area boxes are shown for reference (solid white lines). (b) Relative number of pro-  
 131 files by latitude, scaled by an area-weighting factor  $\cos(\phi)$ , where  $\phi$  is latitude. The temporal distribution of  
 132 profiles shown by (c) month and (d) year.

137 tures in the interior, a physical arrangement that would be unstable to convection without the  
 138 compensating effect of salinity. Profiles around Antarctica tend to be fresher at the surface  
 139 and saltier in the interior due to glacial melt, freshwater flux, and the balance of evapora-  
 140 tion/precipitation. This arrangement of temperature and salinity can be stable to vertical mix-  
 141 ing (called “salt stratification”). In addition, the thermocline, i.e. the region of the ocean that  
 142 features a rapid change in temperature with pressure, is visible in some temperature profiles.

## 146 2.2 Gaussian mixture modeling

147 Gaussian mixture modeling (GMM) is a probabilistic approach for describing and clas-  
 148 sifying data. It attempts to fit (or “model” in the statistical sense) the data as a linear com-  
 149 bination of multi-dimensional Gaussian distributions with unknown means and unknown  
 150 standard deviations. Let  $\mathbf{X}$  be the array of  $N$  vertical profiles, each with  $D$  pressure levels,  
 151 and let  $p(\mathbf{X})$  be the probability distribution function (PDF) representing the entire dataset.



143 **Figure 2.** Plot of 10% of the Argo temperature profiles, chosen at random, in the upper 1000 dbar of the  
 144 cleaned dataset, along with the mean (solid line) and the mean plus or minus one standard deviation (dashed  
 145 lines) across the entire dataset.

152 GMM represents the PDF as a weighted sum of  $K$  Gaussian classes, indexed by  $k$ , i.e.:

$$p(\mathbf{X}) = \sum_{k=1}^K \lambda_k \mathcal{N}(\mathbf{X}; \mu_k, \Sigma_k). \quad (1)$$

153 Here,  $\mathcal{N}(\mathbf{x}; \mu_k, \Sigma_k)$  is the multi-dimensional Gaussian PDF with a vector of means  $\mu_k$  and  
 154 covariance matrix  $\Sigma_k$ , i.e.:

$$\mathcal{N}(\mathbf{x}; \mu_k, \Sigma_k) = \frac{\exp\left[-\frac{1}{2}(\mathbf{x} - \mu_k)^T \Sigma_k^{-1} (\mathbf{x} - \mu_k)\right]}{\sqrt{(2\pi)^D |\Sigma_k|}}. \quad (2)$$

155 The probability associated with class  $k$  is  $p(k) = \lambda_k$ . The probability of profile  $\mathbf{x}$  being in  
 156 class  $k$  is  $p(k|\mathbf{x}) = \lambda_k \mathcal{N}(\mathbf{x}; \mu_k, \Sigma_k) / p(\mathbf{x})$ , where the vector  $\mathbf{x}$  is a single profile taken from  
 157 the complete array  $\mathbf{X}$  and  $p(\mathbf{x})$  is equation (1) with a single profile  $\mathbf{x}$  as the argument, i.e. a  
 158 normalizing factor. Both  $\mathbf{x}$  and  $\mu_k$  are vectors of length  $D$ , and  $\Sigma_k$  is a matrix of size  $D \times D$ .

159 Starting with random initial guesses for the classes, GMM proceeds by iteratively ad-  
 160 justing the means  $\mu_k$  and standard deviations  $\Sigma_k$  (i.e. the “parameters”) of the classes in or-

161 der to maximize a logarithmic measure of likelihood, i.e.:

$$\log[p(\mathbf{X})] = \sum_{i=1}^N \log \left[ \sum_{k=1}^K \lambda_k \mathcal{N}(\mathbf{X}; \mu_k, \Sigma_k) \right]. \quad (3)$$

162 GMM uses an expectation-maximization approach, described in *Maze et al.* [2017]. This  
 163 algorithm monotonically converges on a local maximum. GMM is a generalization of  $k$ -  
 164 means clustering, which only attempts to minimize in-group variance by shifting the means.  
 165 By contrast, GMM attempts to identify means and standard deviations, allowing for some  
 166 variation about the centres of the Gaussian distributions.

167 In our instance of GMM, each pressure level is treated as a “dimension”, and the Gaus-  
 168 sian parameters are associated with each pressure level. However, we may not need all of  
 169 these pressure levels to accurately describe the dataset, as ocean temperature changes much  
 170 more rapidly in the mixed layer and thermocline than in the interior. In order to reduce the  
 171 computational complexity of the problem, we transform the profile data from pressure space  
 172 to an alternative space using principal component analysis (PCA). Specifically, we calculate  
 173 principal components that capture a desired fraction of the vertical variability of the dataset.  
 174 Each eigenvector may be thought of as a “profile type” that describes a certain amount of  
 175 variance in the data with pressure (note that this is not necessarily the same thing as a “typi-  
 176 cal profile”). We calculate  $J$  principal components via the transformation:

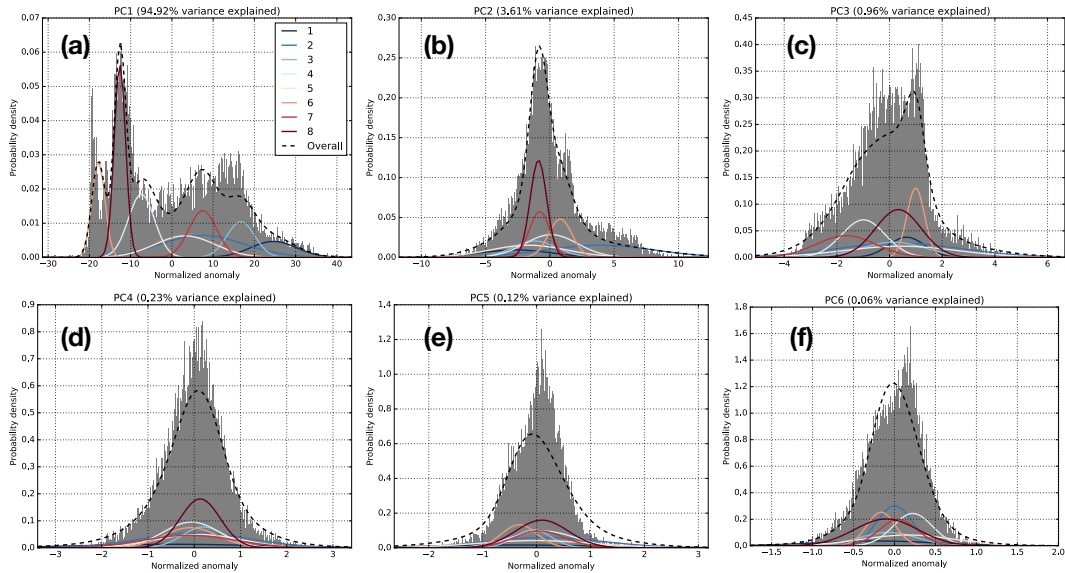
$$\mathbf{X}(z) = \sum_{j=1}^J \mathbf{P}(z, j) \mathbf{Y}(j), \quad (4)$$

177 where  $z$  is the pressure level,  $J$  is the total number of principal components (index  $j$ ), and  
 178  $\mathbf{P}(z, j)$  is the transformation matrix between pressure space and principal component space.  
 179 This strategy is an example of “dimensionality reduction”, which is common in machine  
 180 learning approaches.

181 We find that  $J = 6$  captures 99.9% of the variance in the vertical structure, which  
 182 greatly reduces the number of dimensions needed to describe the Argo profile data used here,  
 183 i.e. from 194 pressure levels to 6 principal components (PCs). We refer to this dataset as  
 184 the “cleaned, compressed” dataset. Nearly 95% of the variance is explained by the first PC  
 185 (i.e. PC1), and the Gaussian functions associated with PC1 are relatively distinct, captur-  
 186 ing the broad shape of the temperature distribution (Figure 3). For higher indexed PCs, the  
 187 Gaussians overlap more, but their sum still makes up a representation of the temperature dis-  
 188 tribution that is sufficiently accurate for our purposes. The fact that we only need six PCs  
 189 to capture 99.9% of the variance is consistent with the strong vertical coherence found in



190 the Southern Ocean, which is well-described by an equivalent barotropic model [Karsten  
 191 and Marshall, 2002]. For more information on the principal components that we used in this  
 192 work, see the supporting information (Figure S1 and S2).



193 **Figure 3.** Probability density functions for the (dimensionless) principal component amplitude coefficients  
 194 associated with each profile, along with the Gaussian functions generated by GMM with  $K = 8$  classes.

195 We used a “training” dataset, a subset of the cleaned, compressed dataset, to estimate  
 196 the parameters (i.e the means and standard deviations) of the GMM classes. To generate the  
 197 GMM training set, we randomly selected a single profile from each  $1^\circ \times 1^\circ$  bin. Each training  
 198 dataset contains 12,286 profiles (roughly 4% of the cleaned, compressed dataset), distributed  
 199 evenly in latitude/longitude space. Note that this sub-selection is not related cross-validation  
 200 analysis, in which there are “training” and “test” datasets [Maze *et al.*, 2017]. Instead, we use  
 201 a random sub-selection that is roughly uniform in latitude-longitude as our test dataset, and  
 202 then we apply the GMM model to the entire cleaned, compressed dataset. As discussed in  
 203 the supporting information, our results are not sensitive to our choice of test dataset.

204 Once we have our test dataset and calculate the optimized parameters (that is, the means  
 205 and standard deviations of the Gaussians), we then statistically represent (i.e. ‘model’) the  
 206 entire cleaned, compressed dataset with the fitted Gaussian model using optimized parame-  
 207 ters. The end result is a probabilistic description of the cleaned, compressed Argo tempera-  
 208 ture profile dataset in terms of a linear combination of Gaussian distributions that vary with  
 209 pressure. Each profile then has a probability distribution across the classes, and the profile is

210 assigned to the class with the highest probability. Our results are not sensitive to our choice  
 211 of training dataset (see supporting information, Table S1).

### 212 **2.2.1 Selecting the number of classes**

213 GMM does have one free parameter, i.e. the maximum number of classes  $K$ . In or-  
 214 der to determine the most appropriate value for  $K$ , we applied a statistical test, namely a  
 215 Bayesian Information Criterion (BIC). BIC uses an empirically formulated cost function that  
 216 rewards likelihood and penalizes the number of classes  $K$ :

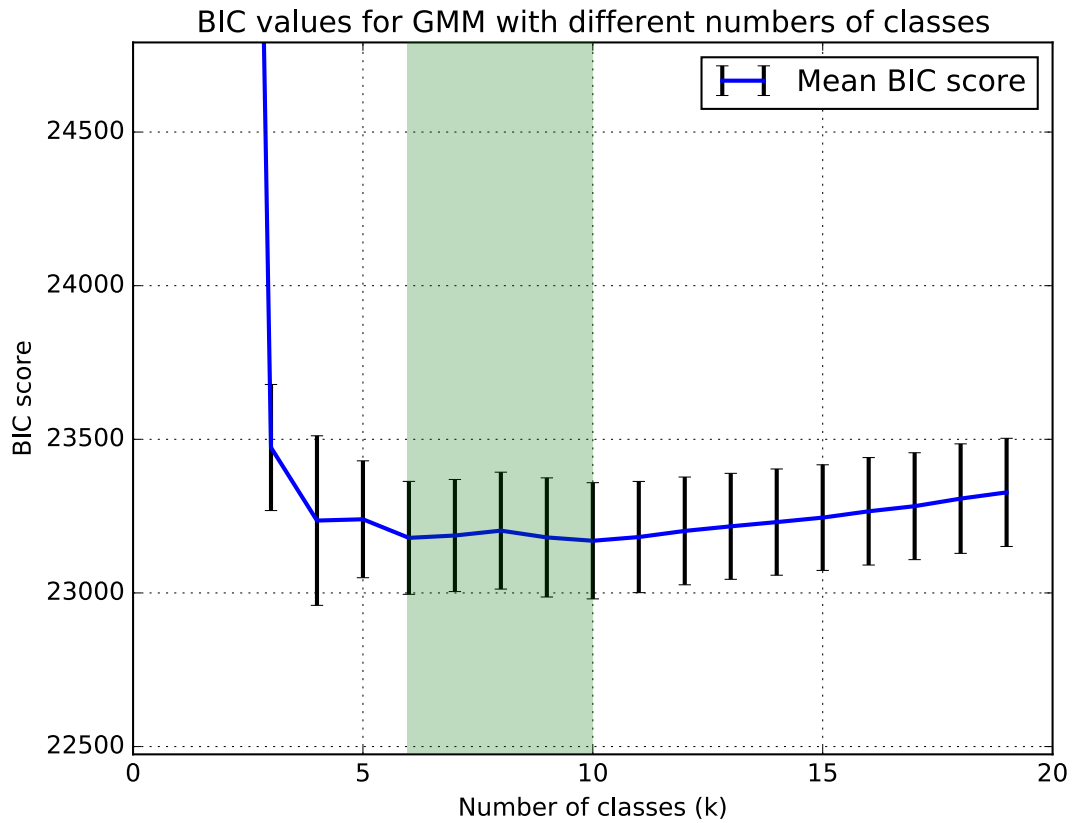
$$BIC(K) = -2\mathcal{L}(K) + N_f(K) \log(n), \quad (5)$$

217 where  $\mathcal{L}$  is a measure of likelihood,  $n$  is the number of profiles used in the BIC test, and  $N_f$   
 218 is the number of independent parameters to be estimated:

$$N_f(K) = K - 1 + KD + \frac{KD(D-1)}{2}. \quad (6)$$

219 In this framework, the optimum value of  $K$  minimizes the BIC score. We perform a number  
 220 of BIC tests, using different subsets of the data and different values of  $K$ , to estimate the dis-  
 221 tribution and variability of BIC. Using the roughly 300 km decorrelation scale of the South-  
 222 ern Ocean as guidance [Ninove *et al.*, 2016], we randomly select a profile from each  $4^\circ \times 4^\circ$   
 223 grid cell, returning 884 random profiles for each BIC test. We calculate BIC scores for each  
 224 set of 884 random profiles (in principal component space) using a range of classes  $K$  from  
 225 1 to 19 (Figure 4). For each value of  $K$ , we repeat the random selection and BIC process 50  
 226 times. BIC analysis does not feature a clear minimum, but instead it suggests that the opti-  
 227 mum value of  $K$  lies between 6 and 10.

232 It may seem counterintuitive that BIC does not return a single optimum value for  $K$ ,  
 233 but this is consistent with the nature of  $K$  as a weakly constrained free parameter that con-  
 234 trols the level of complexity of the statistical description of the dataset. Oceanography has  
 235 a rich history of expertise-driven clustering using physical and biogeochemical criteria (e.g.  
 236 potential vorticity minima, oxygen minima) and the fingerprints of various processes (e.g.  
 237 gyre circulation). These descriptions can be arranged into hierarchies, from coarse/simple  
 238 (e.g. two-layer quasi-geostrophic models) to rich and complex (e.g. the descriptions found  
 239 in Talley [2013]). The level of detail required in the description depends on the application  
 240 at hand. For example, a simple  $\beta$ -plane model is sufficient to explain the existence of gyres  
 241 and western boundary currents; it constitutes a first-order description of gyres. Algorithmic

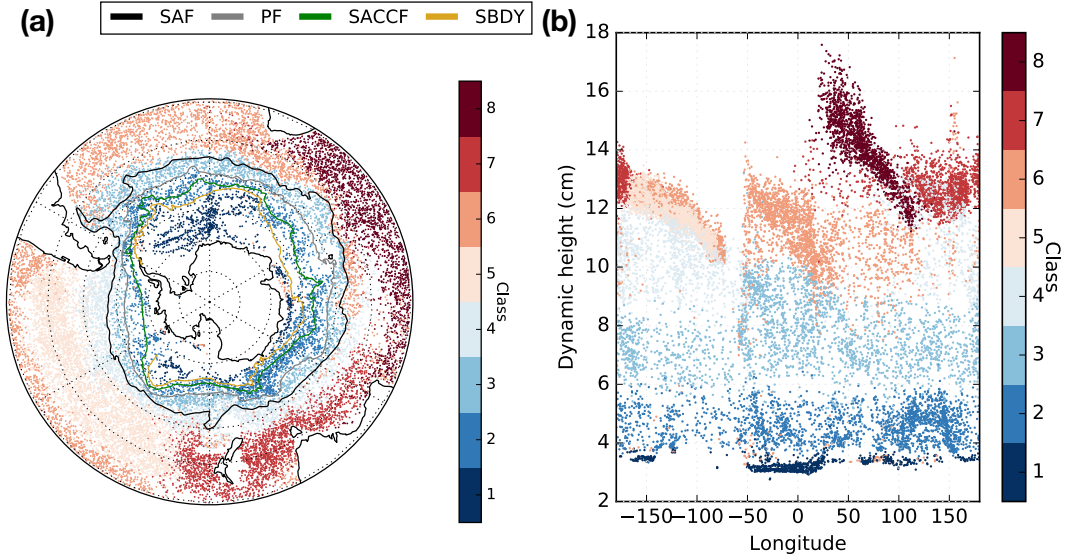


228 **Figure 4.** Bayesian Information Criteria (BIC) scores versus the specified number of classes  $K$ . For each  
 229  $K$ , we calculate the BIC score 50 times using randomly selected profiles as discussed in the text. The means  
 230 (solid blue line) and standard deviations (error bars) are shown for each  $K$ . The range of the smallest mean  $K$   
 231 values is indicated by green shading.

242 clustering offers a robust way to traverse this hierarchy using a range of  $K$  values. Although  
 243 statistical tests can be used as rough guides for choosing the number of classes, there is not  
 244 necessarily a single ideal value for  $K$ . We explore the impact of  $K$  on our results in section 4.

### 245 3 Results

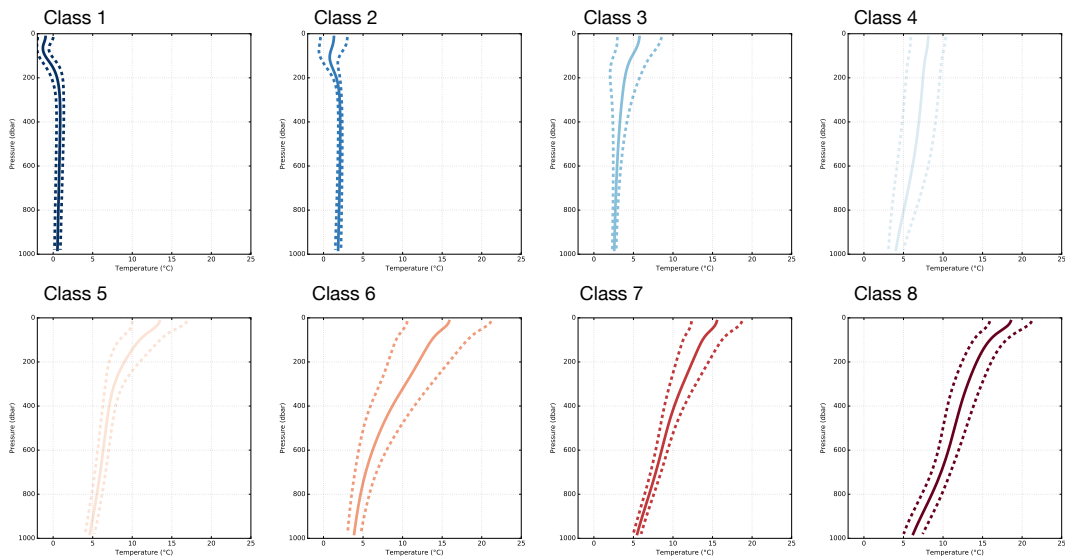
246 In order to identify patterns in the temperature structure of the Southern Ocean, we de-  
 247 scribe the cleaned, compressed Argo temperature profile dataset as a linear combination of  
 248 multi-dimensional Gaussian functions that vary with pressure, using  $K = 8$  different classes.  
 249 Despite the fact that GMM does not have access to the longitudes and latitudes of the pro-  
 250 files, it identifies spatially coherent structures, some of which are roughly demarcated by the  
 251 fronts of the ACC as defined by *Kim and Orsi [2014]* (Figure 5). For ease of interpretation,  
 252 we sorted the classes by mean temperature (Table 1).



253 **Figure 5.** (a) GMM-derived class distribution for  $K = 8$ , shown with four fronts of the Antarctic Circum-  
 254 polar Current, i.e. the Subantarctic Front (SAF), Polar Front (PF), Southern ACC Front (SACCF), and the  
 255 Southern Boundary (SBDY) [Kim and Orsi, 2014]. (b) Class distribution shown in dynamic height space  
 256 ( $\phi_{1500\text{dbar}}^{300\text{dbar}}$ ). Note that only points with posterior probability  $\geq 0.9$  are shown. The classes are sorted by mean  
 257 temperature, from coldest ( $k = 1$ ) to warmest ( $k = 8$ ).

258 The class nearest Antarctica (class 1) extends throughout the Weddell Gyre and coastal  
 259 Antarctica (Figure 5a). The mean temperature profile in this region is inverted, that is, it is  
 260 colder near the surface and warmer in the interior (Figure 6). This near-Antarctic class coin-  
 261 cides with regions of Antarctic Bottom Water (AABW) export [Orsi *et al.*, 1999; Ohshima  
 262 *et al.*, 2013], the subpolar Weddell and Ross gyres, and its northern extent approximately cor-  
 263 responds with the classical Southern Boundary (SBDY) of the ACC [Kim and Orsi, 2014].  
 264 This class occupies a narrow range in dynamic height space, with a class mean and standard  
 265 deviation of  $3.3 \pm 0.2$  cm ( $\phi_{1500\text{dbar}}^{300\text{dbar}}$ , Figure 5b); it is fairly distinct from the other classes, that  
 266 is, class 1 profiles are rarely found north of the SBDY. For reference, Kim and Orsi [2014]  
 267 associate the SBDY with the 3.1 cm dynamic height contour ( $\phi_{1500\text{dbar}}^{500\text{dbar}}$ ). As their limits of  
 268 integration over pressure are different than ours, this value of dynamic height is not directly  
 269 applicable to our data, but it is roughly consistent with the gap between classes 1 and 2 in  
 270 our analysis (Figure 5b). Assuming that the data features sufficiently uniform spatial cov-  
 271 erage, gaps in dynamic height space may be indicative of fronts, as they may suggest sharp  
 272 gradients in dynamic height over relatively short physical distances. We do not pursue this

273 analysis further here. For an in-depth analysis of SO front positions, see *Sokolov and Rintoul*  
 274 [2009], for example.



275 **Figure 6.** Temperature profile statistics, separated by class, as functions of pressure. Shown are the mean  
 276 (solid lines) and the mean plus or minus one standard deviation (dashed lines) for all profiles in the indicated  
 277 class.

278 The second coldest class (class 2) is a circumpolar class with profiles that sit north of  
 279 the SBDY and south of the Polar Front (PF) across all longitudes; it is the dominant class in  
 280 the dynamic height range 4-6 cm, with a class mean value of  $4.8 \pm 0.7$  cm ( $\phi_{1500\text{dbar}}^{300\text{dbar}}$ , Fig-  
 281 ure 5). Its mean profile is also inverted, though not as sharply as the mean profile of class  
 282 1 (Figure 6). A second circumpolar class (class 3) sits roughly north of the PF and south of  
 283 the Subantarctic Front (SAF). In dynamic height space, class 3 is found between roughly 6-8  
 284 cm, except in the Atlantic sector, where it extends to roughly 10 cm. For reference, *Kim and*  
 285 *Orsi* [2014] associate the PF with the 5.0 cm dynamic height contour and the SAF with the  
 286 7.0 cm dynamic height contour ( $\phi_{1500\text{dbar}}^{500\text{dbar}}$ ). These values are roughly consistent with (but not  
 287 directly comparable to) the gap positions in our data. Unlike the first two classes, the mean  
 288 profile of class 3 is not inverted, that is, it gets colder with pressure. The presence of these  
 289 two circumpolar classes is consistent with the homogenizing influence of the ACC, which  
 290 typically encourages mixing along the strong jets associated with fronts and suppresses mix-  
 291 ing across them [*Ferrari and Nikurashin*, 2010].

292 The profiles assigned to class 4 are mostly located north of the SAF in the Pacific and  
293 Indian sectors, roughly coinciding with regions of Subantarctic Mode Water (SAMW) and  
294 Antarctic Intermediate Water (AAIW) formation in the Pacific Ocean and south of Australia  
295 [Sallée *et al.*, 2010b]. Despite its relatively narrow range in latitude, class 4 profiles occupy  
296 a broad, distinct range in dynamic height space in the Pacific Sector, with a class mean of  
297  $11 \pm 1.5$  cm. The mean vertical profile associated with class 4 changes relatively gently with  
298 pressure, with no clear thermocline and a relatively large standard deviation across all pres-  
299 sures.

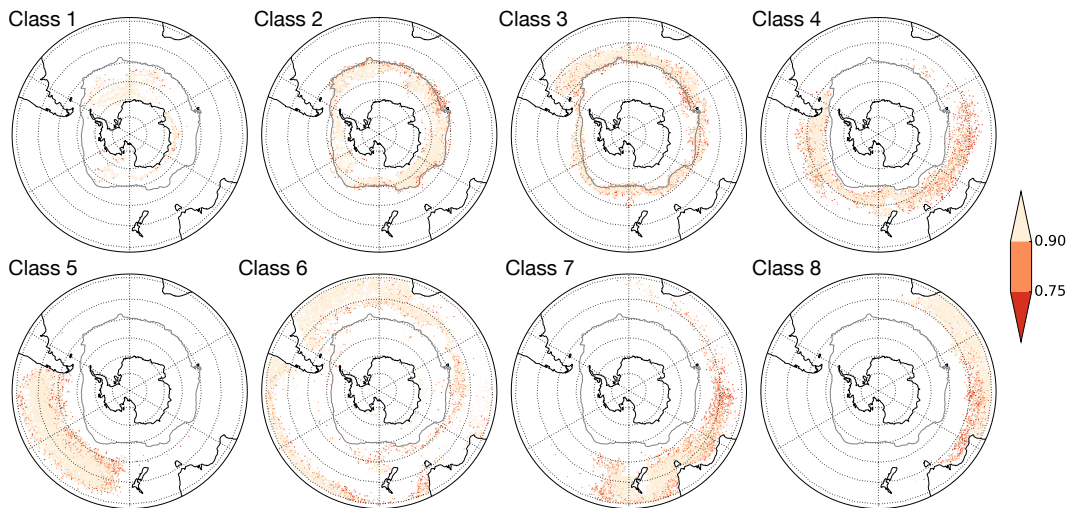
300 Profiles assigned to class 5 are mostly found in the Pacific Sector, in a region associ-  
301 ated with the export of SAMW and AAIW from the surface ocean into the interior thermo-  
302 cline [Judicone *et al.*, 2007; Jones *et al.*, 2016]. In contrast with class 4, class 5 occupies a  
303 relatively large range in latitude and a relatively small range in dynamic height, with a mean  
304 and standard deviation of  $12 \pm 0.7$ cm. The mean vertical profile has a clear thermocline over  
305 the upper 400 dbar of the ocean, with a standard deviation that narrows considerably with  
306 pressure. This class spatially coincides with the southern part of the South Pacific gyre, sug-  
307 gesting that gyre circulation tends to homogenize properties in this region.

308 Class 6 highlights warmer subtropical waters and is mostly found in the Atlantic and  
309 Pacific sectors; it partially extends into the Indian sector, where it sits just north of the SAF.  
310 From the surface to well into the interior, class 6 features some of the largest standard devia-  
311 tions of any class, suggesting that class 6 consists of a wide variety of profiles; it can poten-  
312 tially be split into a number of smaller classes. Classes 7 and 8 are also warmer subtropical  
313 classes, with class 7 found mostly near Australia and New Zealand and class 8 found almost  
314 exclusively in the Indian sector. Much of class 8 spatially coincides with the Indian Ocean  
315 gyre. The spatial extent of class 8 near South Africa suggests that the Agulhas current influ-  
316 ences the temperature structure in that region. The mean vertical profiles of classes 7 and 8  
317 are similar, although class 7 features higher variability near the surface and class 8 features  
318 slightly warmer surface temperatures. The higher variability in class 7 may be due to the  
319 overlap of profiles in this class with a wider range of surface current features (e.g. boundary  
320 currents around Australia and New Zealand, whereas class 8 largely overlaps with the Indian  
321 Ocean gyre.

322 For a selected temperature profile, GMM predicts the probability distribution across  
323 all  $K$  classes. That is, it calculates the probabilities that the profile belongs to each class  $k$ .

324 Next, the algorithm assigns the profile to the class with the highest probability. Note that  
 325 the sum of the posterior probabilities across all classes is one. Since these probabilities are  
 326 calculated with the full data set available, they are referred to as posterior probabilities. The  
 327 posterior probabilities are useful in their own right, as measures of confidence in GMM's  
 328 assignment of a profile to a particular class.

329 For our implementation of GMM on Argo temperature data, over 86% of the class as-  
 330 signments have posterior probabilities greater than 0.75, and over 74% of all class assign-  
 331 ments have posterior probabilities greater than 0.9 (Table 2). Class 1 features an especially  
 332 high percentage of very high posterior probabilities; over 90% of assignments into class  
 333 1 have posterior probabilities greater than or equal to 0.9. Outside of the Weddell Gyre,  
 334 we find the lowest posterior values in the Ross Sea and a few near-coastal areas (Figure 7).  
 335 The low posterior values could possibly be due to seasonal variability that is not well repre-  
 336 sented by a single class. Classes 2 and 3 also feature high posterior probabilities, for which  
 337 over 70% of assignments have values greater than or equal to 0.9. For both of these classes,  
 338 we find relatively low posterior probabilities upstream of Kerguelen Island (KI), clustered  
 339 around the PF. The area around KI is affected by upwelling, mixing, and the confluence of  
 340 the Agulhas Retroflexion and the ACC [Sallée *et al.*, 2010b], and it also features relatively  
 341 high eddy diffusivities [Klocker and Abernathy, 2014]. The profiles in that area are influ-  
 342 enced by a number of competing processes and may be difficult to unambiguously separate  
 343 into clear groups when using a value of  $K$  appropriate for the entire Southern Ocean.



344 **Figure 7.** Posterior probabilities for each class assignment, given the full cleaned, compressed dataset,  
 345 shown together with the PF for reference [Kim and Orsi, 2014].

346 Although over 60% class 4 profiles have posterior values greater than or equal to 0.9,  
 347 class 4 features some relatively low posterior values compared with the other classes, es-  
 348 pecially in the Indian sector north of the SAF. In the Pacific sector, we find relatively low  
 349 posteriors along the boundary between classes 4 and 5. Class 5 has a core of profiles with  
 350 posterior values greater than or equal to 0.9, with relatively lower values all along its bound-  
 351 ary. We find similar patterns for classes 6-8, except in the Indian sector between 60-120° E,  
 352 north of the SAF. This region, which is downstream of Kerguelen Plateau, is characterized  
 353 by relatively low posterior values for classes 4, 7, and 8. In general, although GMM performs  
 354 well in all ocean basins, in terms of clear class separation with high posterior probabilities,  
 355 its performance is somewhat weaker in the Indian sector.

## 356 **4 Discussion**

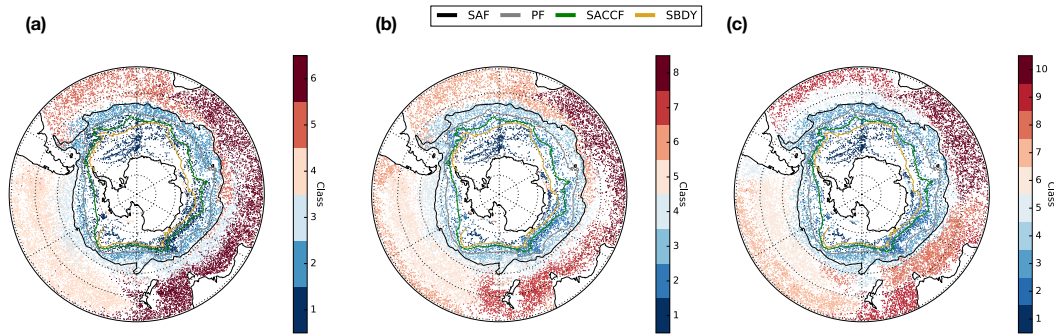
357 Here we explore the sensitivity of our results to the maximum number of classes  $K$ .  
 358 We also explore a possible alternative to PCA that may be useful for incorporating salinity  
 359 into our analysis, namely functional PCA.

### 360 **4.1 Sensitivity to number of classes $K$**

361 In section 2, we estimated that the optimum number of classes  $K$  lies between 6 and  
 362 10. The weak constraint suggested by BIC allows for some tuning depending on the desired  
 363 level of complexity in the description of the dataset. Using  $K = 6$  classes is sufficient to cap-  
 364 ture most of the large-scale structures identified in the  $K = 8$  case, but there are some signif-  
 365 icant differences (Figure 8a,b). Specifically, there is one fewer circumpolar class, as classes  
 366 1-3 are reduced to classes 1-2 that sit roughly on either side of the PF. In the Pacific sector,  
 367 classes 4 and 5 merge into the new class 4. In the Indian sector, classes 7-8 merge into the  
 368 new class 6 that sits north of the SAF and south of Australia. We see that the overall descrip-  
 369 tion of ocean structure is simpler with  $K = 6$ ; it is still a physically reasonable description of  
 370 ocean temperature structure, with circumpolar classes and clusters that span the major basins,  
 371 but it lacks some of the subtleties found in the  $K = 8$  map.

374 As expected, the  $K = 10$  case features more structure than the  $K = 8$  case, and it is still  
 375 a physically reasonable distribution (Figure 8b,c). Classes 1-3 are still near-Antarctic or cir-  
 376 cumpolar classes; the additional structure all appears north of the SAF. In the Pacific basin,  
 377 the boundary between the  $K = 8$  classes 5 and 6 and the  $K = 10$  classes 6 and 7 is shifted





372 **Figure 8.** Comparison of GMM-derived classes, shown for (a) 6 classes, (b) 8 classes, and (c) 10 classes,  
 373 along with fronts of the ACC [Kim and Orsi, 2014].

378 polewards, and a new class 5 is found along the Eastern Pacific, along the South American  
 379 coast. The  $K = 10$  class 8 is found south of Australia, which in the  $K = 8$  class is not a  
 380 distinct class. Interestingly, in the  $K = 10$  case we find more profiles above 0.9 posterior  
 381 probability in the Indian sector, specifically in the region north of the SAF and between the  
 382 longitudes of 60-120°E. Increasing  $K$  allowed for a more likely set of class assignments in  
 383 this previously troublesome region. So, regions of low posterior probabilities may suggest a  
 384 need for a higher value of  $K$ .

#### 385 4.2 Including additional variables

386 In this work, we define classes using temperature profiles. A more general descrip-  
 387 tion of ocean structure may include some combination of additional fields (e.g. salinity, den-  
 388 sity, potential vorticity, and biogeochemical variables). Including additional variables in the  
 389 GMM analysis is not necessarily trivial, as there are different approaches, and each approach  
 390 has advantages and limitations that need to be thoroughly evaluated. Perhaps the simplest  
 391 approach is to standardize the additional variables in the same way as the temperature fields,  
 392 such that each field is expressed in terms of standard deviations relative to the mean at each  
 393 depth level. This approach has the potential disadvantage that a  $1\sigma$  variation in temperature  
 394 has the same impact on class structure as a  $1\sigma$  variation in salinity, which is not necessarily  
 395 physically realistic. Statistically similar variations in temperature and salinity need not have  
 396 similar impacts on ocean structure. Another approach is to scale by parameters from the lin-  
 397 ear equation of state (EOS), namely the thermal expansion coefficient  $\alpha$  for temperature and  
 398 the coefficient of haline contraction  $\beta$  for salinity. Using this method, variations in tempera-

399 ture and salinity would impact density in a manner that is physically constrained by the EOS,  
400 i.e.  $\rho = \rho_0 [1 - \alpha(T - T_0) + \beta(S - S_0)]$ . However, this approach would only be valid in the  
401 neighborhood of the reference values  $(T_0, S_0)$  in T-S space, over which the linear EOS is a  
402 good approximation of the full, nonlinear EOS. This limitation would likely be problematic  
403 in the Southern Ocean, where nonlinear terms in the EOS play an important role in the for-  
404 mation and layering of Antarctic Intermediate Water and Antarctic Bottom Water [Nycander  
405 *et al.*, 2015]. Still another approach would be to classify profiles based on density, but there  
406 are a number of different approaches to defining density that would need to be treated with  
407 care (e.g.  $\sigma_0$ ,  $\sigma_1$ , neutral density  $\gamma_n$ ).

408 We used PCA to reduce the dimensionality of our Argo temperature profile dataset. An  
409 alternative approach is to use functional principal component analysis (fPCA), in which PCA  
410 is performed on functions instead of the original data. In Pauthenet *et al.* [2017], the authors  
411 represent vertical temperature and salinity profiles from the Southern Ocean State Estimate  
412 [Mazloff *et al.*, 2010] as linear combinations of B-spline basis functions and apply fPCA to  
413 the resulting spline functions. They use the principal components to examine large-scale  
414 structures such as fronts in the Southern Ocean. Their approach offers another objective way  
415 to define structural boundaries and could be used in concert with the GMM approach out-  
416 lined in this work. This could offer yet another possible way to introduce salinity into the  
417 GMM analysis, which is especially relevant for stratification south of the PF [Pollard, 2002].

## 418 5 Conclusions

419 We applied GMM, an unsupervised classification scheme, to Southern Ocean Argo  
420 temperature data above 1000 dbar. Without using longitude or latitude information, GMM  
421 identified spatially coherent patterns in the vertical temperature structure. The GMM-derived  
422 classes broadly coincide with large-scale circulation and stratification features, including re-  
423 gions of AABW formation and upwelling (i.e. adjacent to Antarctica), the ACC, formation  
424 and export pathways of SAMW and AAIW, subtropical gyre circulation, and the Agulhas  
425 Current and associated retroflexion. We may say that GMM identifies *domains* in oceanographic  
426 data, including gyre-dominated domains and circumpolar domains, among others.  
427 GMM can be used to define these domains in a method that respects the structure of the  
428 data, as opposed the simpler but physically unrealistic process of defining domains by simply  
429 drawing rectangular boxes in latitude-longitude space. GMM also makes use of the interior  
430 structure of the data, as opposed to only using surface variables like SSH. The class bound-

431 aries broadly coincide with several classically-defined fronts of the ACC, and the circumpo-  
432 lar classes mostly occupy distinct regions in dynamic height space, indicating that GMM has  
433 identified physically distinct profile types using only vertical temperature data. High poste-  
434 rior probability distributions indicate regions where the classes are distinct and statistically  
435 separate, whereas regions with low posterior probability indicate boundaries between classes  
436 and/or regions of mixing influenced by a number of different temperature structures. GMM  
437 may offer an alternative, complementary method for describing Southern Ocean spatial vari-  
438 ability, and it is potentially useful for objectively and automatically comparing structures  
439 across different observational and modeling datasets.

Class	Number of profiles	Mean	Std. dev.	Min.	Max.
1	10680	0.48	0.81	-2.11	2.52
2	33031	1.83	0.72	-1.87	8.89
3	40268	3.38	1.50	-1.82	19.70
4	39619	6.36	2.24	-1.85	17.17
5	48252	7.32	2.56	2.76	25.37
6	48770	8.22	4.49	-1.88	27.56
7	38682	9.70	3.07	3.25	27.11
8	25130	11.57	3.43	3.56	28.08

440 **Table 1.** Temperature statistics for each class, using values from every pressure level. All temperature statis-  
441 tics are shown in °C. The classes have been sorted by mean temperature, calculated using values from all  
442 pressure levels.

Class	[0.0, 0.50)	[0.50, 0.75)	[0.75, 0.9)	[0.9, 1.0]
1	<1	4	4	91
2	<1	11	11	77
3	<1	14	16	70
4	1	18	20	61
5	<1	7	8	84
6	<1	9	8	82
7	<1	19	17	64
8	<1	13	12	75

443 **Table 2.** Posterior probabilities for each class, divided into four unequal intervals. Each row shows the  
444 percentage of profiles assigned to that class with posterior probabilities in the indicated range.

## 445 Acronyms

446 **AABW** Antarctic Bottom Water

447 **AAIW** Antarctic Intermediate Water

448 **ACC** Antarctic Circumpolar Current

449 **BIC** Bayesian Information Criterion

450 **fPCA** Functional principal component analysis

451 **GDAC** Global Data Assembly Center  
452 **GMM** Gaussian mixture modeling  
453 **PC** Principal component  
454 **PCA** Principal component analysis  
455 **PDF** Probability distribution function  
456 **SAMW** Subantarctic Mode Water

## 457 **Acknowledgments**

458 This study is supported by grants from the Natural Environment Research Council (NERC),  
459 including [1] The North Atlantic Climate System Integrated Study (ACSIS) [grant NE/N018028/1  
460 (authors DJ, ES)] and [3] Ocean Regulation of Climate by Heat and Carbon Sequestration  
461 and Transports (ORCHESTRA) [grant NE/N018095/1 (authors ES, AM)]. HH was funded  
462 by a NERC DTP Research Experience Placement over the summer of 2017 [grant NE/L002434/1].  
463 Argo floats data were collected and made freely available by the International Argo Pro-  
464 gram and the national programs that contribute to it. (<http://www.argo.ucsd.edu> and  
465 <http://argo.jcommops.org>). The Argo Program is part of the Global Ocean Observing  
466 System. Argo floats data and metadata are available from the Global Data Assembly Cen-  
467 tre (Argo GDAC), <http://doi.org/10.17882/42182>. The analysis software used in this  
468 manuscript was written using Python and the *scikit-learn* machine learning library ([http://](http://scikit-learn.org/stable/)  
469 [scikit-learn.org/stable/](http://scikit-learn.org/stable/)). Version 1.0 of the scripts we used are available via github  
470 (<https://github.com/DanJonesOcean/OceanClustering/releases/tag/v1.0>). DJ  
471 thanks Chris Lowder for python support. We are grateful to Y.S. Kim for providing us with  
472 Southern Ocean front position data. Finally, we thank Guillaume Maze and three anonymous  
473 reviewers, whose feedback greatly improved the quality of our work.

## 474 **References**

475 Emery, W. J. (2003), Water Types and Water Masses, in *Encyclopedia of Atmospheric*  
476 *Sciences*, edited by J. R. Holton, J. A. Curry, and J. A. Pyle, pp. 1556–1567, Elsevier,  
477 doi:10.1016/b0-12-227090-8/00279-7.  
478 Ferrari, R., and M. Nikurashin (2010), Suppression of eddy diffusivity across jets  
479 in the Southern Ocean, *Journal of Physical Oceanography*, *40*, 1501–1519,  
480 doi:10.1175/2010JPO4278.1.

- 481 Fletcher, S. M., N. Gruber, A. R. Jacobson, S. C. Doney, S. Dutkiewicz, M. Gerber, M. Fol-  
482 lows, F. Joos, K. Lindsay, D. Menemenlis, A. Mouchet, S. A. Müller, and J. L. Sarmiento  
483 (2006), Inverse estimates of anthropogenic CO<sub>2</sub> uptake, transport, and storage by the  
484 ocean, *Global Biogeochemical Cycles*, 20, doi:10.1029/2005gb002530.
- 485 Frölicher, T. L., J. L. Sarmiento, D. J. Paynter, J. P. Dunne, J. P. Krasting, and M. Winton  
486 (2015), Dominance of the Southern Ocean in Anthropogenic Carbon and Heat Uptake in  
487 CMIP5 Models, *Journal of Climate*, 28(2), 862–886, doi:10.1175/jcli-d-14-00117.1.
- 488 Hanawa, K., and L. Talley (2001), Mode Waters, in *Ocean Circulation and Climate*, edited  
489 by G. Siedler and J. Church, pp. 373–386, International Geophysics Series.
- 490 Herraiz-Borreguero, L., and S. R. Rintoul (2011), Subantarctic mode water: distribution and  
491 circulation, *Ocean Dynamics*, 61(1), 103–126, doi:10.1007/s10236-010-0352-9.
- 492 Holt, H. J., and D. C. Jones (2018), Southern Ocean temperature profile classification tool,  
493 doi:10.5281/zenodo.1543106.
- 494 Iudicone, D., K. Rodgers, R. Schopp, and G. Madec (2007), An exchange window for the  
495 injection of Antarctic Intermediate Water into the South Pacific, *Journal of Physical*  
496 *Oceanography*, 37, 31–49, doi:http://dx.doi.org/10.1175/JPO2985.1.
- 497 Jones, D. C., A. J. S. Meijers, E. Shuckburgh, J.-B. Sallée, P. Haynes, E. K. McAufield,  
498 and M. R. Mazloff (2016), How does Subantarctic Mode Water ventilate the Southern  
499 Hemisphere subtropics?, *Journal of Geophysical Research - Oceans*, 121(9), 6558–6582,  
500 doi:10.1002/2016jc011680.
- 501 Karsten, R. H., and J. Marshall (2002), Constructing the residual circulation of the ACC  
502 from observations, *Journal of Physical Oceanography*, 32, 3315–3327, doi:10.1175/1520-  
503 0485(2002)032<3315:CTRCOT>2.0.CO;2.
- 504 Kim, Y. S., and A. H. Orsi (2014), On the Variability of Antarctic Circumpolar Current  
505 Fronts Inferred from 1992–2011 Altimetry\*, *Journal of Physical Oceanography*, 44(12),  
506 3054–3071, doi:10.1175/JPO-D-13-0217.1.
- 507 Klocker, A., and R. Abernathey (2014), Global Patterns of Mesoscale Eddy Properties and  
508 Diffusivities, *Journal of Physical Oceanography*, 44(3), 1030–1046, doi:10.1175/jpo-d-  
509 13-0159.1.
- 510 Lumpkin, R., and K. Speer (2007), Global ocean meridional overturning, *Journal of Physical*  
511 *Oceanography*, 37, 2550–2562, doi:10.1175/JPO3130.1.
- 512 Maze, G., H. Mercier, R. Fablet, P. Tandeo, M. L. Radenco, P. Lenca, C. Feucher, and  
513 C. Le Goff (2017), Coherent heat patterns revealed by unsupervised classification of Argo

- 514 temperature profiles in the North Atlantic Ocean, *Progress in Oceanography*, 151, 275–  
515 292, doi:10.1016/j.pocean.2016.12.008.
- 516 Mazloff, M. R., P. Heimbach, and C. Wunsch (2010), An Eddy-Permitting South-  
517 ern Ocean State Estimate, *Journal of Physical Oceanography*, 40(5), 880–899,  
518 doi:10.1175/2009jpo4236.1.
- 519 Naveira-Garabato, A. C. N., L. Jullion, D. P. Stevens, K. J. Heywood, and B. A. King (2009),  
520 Variability of Subantarctic Mode Water and Antarctic Intermediate Water in the Drake  
521 Passage during the Late-Twentieth and Early-Twenty-First Centuries, *Journal of Climate*,  
522 22(13), 3661–3688, doi:10.1175/2009jcli2621.1.
- 523 Naveira-Garabato, A. C. N., R. Ferrari, and K. L. Polzin (2011), Eddy stirring in the South-  
524 ern Ocean, *Journal of Geophysical Research*, 116(C9), doi:10.1029/2010jc006818.
- 525 Ninove, F., P. Y. Le Traon, E. Remy, and S. Guinehut (2016), Spatial scales of temperature  
526 and salinity variability estimated from Argo observations, *Ocean Science*, 12(1), 1–7,  
527 doi:10.5194/os-12-1-2016.
- 528 Nycander, J., M. Hieronymus, and F. Roquet (2015), The nonlinear equation of state of sea  
529 water and the global water mass distribution, *Geophysical Research Letters*, 42(18), 7714–  
530 7721, doi:10.1002/2015GL065525.
- 531 Ohshima, K. I., Y. Fukamachi, G. D. Williams, S. Nishihashi, F. Roquet, Y. Kitade, T. Tamura,  
532 D. Hirano, L. Herraiz-Borreguero, I. Field, M. Hindell, S. Aoki, and M. Wakatsuchi  
533 (2013), Antarctic Bottom Water production by intense sea-ice formation in the Cape Darn-  
534 ley polynya, *Nature Geoscience*, 6(3), 235–240, doi:10.1038/ngeo1738.
- 535 Orsi, A., T. Whitworth, and W. Nowlin (1995), On the meridional extent and fronts of the  
536 Antarctic Circumpolar Current, *Deep Sea Research Part I*, 42(5), 641–673.
- 537 Orsi, A. H., G. C. Johnson, and J. L. Bullister (1999), Circulation, mixing, and production of  
538 Antarctic Bottom Water, *Progress in Oceanography*, 43(1), 55–109, doi:10.1016/s0079-  
539 6611(99)00004-x.
- 540 Pauthenet, É., F. Roquet, G. Madec, and D. Nerini (2017), A linear decomposition of the  
541 Southern Ocean thermohaline structure, *Journal of Physical Oceanography*, 47, 29–47,  
542 doi:10.1175/JPO-D-16-0083.s1.
- 543 Pollard, R. T., M. I. Lucas, and J. F. Read (2002), Physical controls on biogeochemi-  
544 cal zonation in the Southern Ocean, *Deep Sea Research Part II*, 49(16), 3289–3305,  
545 doi:10.1016/S0967-0645(02)00084-X.

- 546 Purkey, S. G., and G. C. Johnson (2010), Warming of Global Abyssal and Deep Southern  
 547 Ocean Waters between the 1990s and 2000s: Contributions to Global Heat and Sea Level  
 548 Rise Budgets\*, *Journal of Climate*, 23(23), 6336–6351, doi:10.1175/2010jcli3682.1.
- 549 Sallée, J., R. Morrow, and K. Speer (2008), Eddy heat diffusion and Subantarctic Mode Wa-  
 550 ter formation, *Geophysical Research Letters*.
- 551 Sallée, J., K. Speer, S. Rintoul, and S. Wijffels (2010a), Southern Ocean thermocline ventila-  
 552 tion, *Journal of Physical Oceanography*, 40, 509–529, doi:10.1175/2009JPO4291.1.
- 553 Sallée, J., E. Shuckburgh, N. Bruneau, A. Meijers, T. Bracegirdle, Z. Wang, and T. Roy  
 554 (2013), Assessment of Southern Ocean water mass circulation and characteristics in  
 555 CMIP5 models: historical bias and forcing response, *Journal of Research: Oceans*, 118,  
 556 1830–1844, doi:10.1002/jgrc.20135.
- 557 Sallée, J.-B., K. Speer, S. Rintoul, and S. Wijffels (2010b), Southern Ocean Ther-  
 558 mocline Ventilation, *Journal of Physical Oceanography*, 40(3), 509–529,  
 559 doi:10.1175/2009jpo4291.1.
- 560 Sokolov, S., and S. R. Rintoul (2009), Circumpolar structure and distribution of the Antarc-  
 561 tic Circumpolar Current fronts: 1. Mean circumpolar paths, *Journal of Geophysical Re-  
 562 search: Atmospheres*, 114(C11), 3675, doi:10.1029/2008JC005108.
- 563 Talley, L. (2013), Closure of the Global Overturning Circulation Through the Indian, Pa-  
 564 cific, and Southern Oceans: Schematics and Transports, *Oceanography*, 26(1), 80–97,  
 565 doi:10.5670/oceanog.2013.07.